Transparent and Conductive Polyimide-Ionene Hybrid Interlayers for High Performance and Cost-Effective Semi-Transparent Organic Solar Cells

Zuhao You,[a] Junjie Wen,[a] Wenxu Liu,[a] Zachary Fink,[b] Xuefei Wu,[c] Hong-Gyu Seong,[b] Yuxing Wang,[a] Lei Zhang,[a] Xu Wang,[a] Thomas P. Russell,[b] and Yao Liu*[a]*

[a] State Key Laboratory of Chemical Resource Engineering, Beijing Advanced Innovation Center for Soft Matter Science and Engineering, College of Chemistry, Beijing University of Chemical Technology, Beijing, 100029, China
E-mail: liuyao@mail.buct.edu.cn; liuwenxu@mail.buct.edu.cn

[b] Polymer Science and Engineering Department, University of Massachusetts Amherst, 120 Governors Drive, Amherst, MA 01003, USA.

[c] Materials Sciences Division, Lawrence Berkeley National Laboratory, Berkeley, CA 94720, USA.

Keywords: Polyimide-ionene hybrids, Interlayers, Transparency, Conductivity, Organic solar cells

Abstract

The contradiction between high transmittance and favorable conductivity poses a great challenge in developing effective cathode interlayer (CIL) materials with sufficient thickness tolerance, which hinders further advancement of organic solar cells (OSCs). Herein, we propose a completely new class of alcohol processable polyimide-ionene hybrids (PIIHs) by melding pyromellitic diimide (PMD) subunits into imidazolium-based ionenes backbone covalently. These PIIHs, named PMD-DI and PMD-PD, boast high transparency, suitable energy levels, and decent conductivity. A higher PMD content endows PMD-PD with improved work function tunability, electrical properties, and crystallinity, enabling PMD-PD as CIL material with excellent thickness-insensitive characteristics, while simultaneously improving device stability significantly. Furthermore, PMD-PD also exhibits good compatibility with various electrodes and active layers, offering solar cell efficiencies up to 19.91% and 19.29% with Ag and Cu cathodes, respectively. More importantly, the application of PMD-PD can improve the performance of semi-transparent OSCs without losing transmittance, thereby drastically enhancing the light utilization efficiency to 4.04% with an ultrathin, low-cost Cu cathode, that competes with leading optical modulation-free semi-transparent OSCs with expensive Ag cathodes. This work opens a pathway to realize transparent and conductive interlayers by strategically molecular design, leading to highly efficient, stable, and cost-effective OSCs suitable for diverse applications.

1. Introduction

Organic solar cells (OSCs) have attracted considerable attention due to their light weight, flexibility, transparency, and compatibility with large-scale and low-cost solution processing.[1-5] Significant efforts have been dedicated to improving the power conversion efficiencies (PCEs) of the OSCs by advancing active layer materials and optimizing device fabrication technology, signaling a favorable outlook towards the commercial viability.[6-14] A key factor in achieving a high PCE is facilitating efficient charge transport between the active layer and the electrode.[15] Interface engineering, involving the design and integration of functional interlayers into devices, is recognized as a crucial strategy for aligning energy levels and eliminating interfacial energy barriers to enhance the charge transport and collection in OSCs.[16-18]

It is known that ideal interlayers should have high optical transparency, a capability to tune the electrode work function (*WF*), and excellent charge carrier mobility and conductivity.[19-22] These traits are essential not only for large-scale industrial manufacturing, where precise control over film thickness is challenging, but also for meeting the prerequisites for the market deployment of OSCs, notable in semi-transparent solar cell devices (ST-OSCs), which have distinct applications in multifunctional power-generating windows and photovoltaic-based greenhouses.[23-25] Poly(3,4-ethylenedioxythiophene):poly(styrenesulfonate) (PEDOT:PSS), a widely used conductive polymers complex, exhibits these attributes and has been successfully used as a thickness-insensitive anode interlayer (AIL) material with an optimal thickness of ~30 nm.[26] However, the development of cathode interlayer (CIL) materials necessitates addressing the delicate balance between optical transparency and electron transport. Amine-substituted polyfluorene (PFN) and poly(ethyleneimine) (PEI) derivatives serve as exemplary CILs with high transparency.[27,28] Yet, the p-type PFN backbone, and insulating nature of PEI severely hinder electron transport. To address this, the conventional approach involves incorporating π-extended electron-withdrawing units like naphthalene diimides (NDIs), perylene diimides (PDIs), and functional fullerenes, which can markedly enhance electrical conductivity. Nevertheless, this strategy tends to reduce the bandgap and increase light absorption within the interlayers simultaneously, potentially competing with the absorption of the active layers.[29-31] Consequently, most cutting-edge CILs still offer narrow processing windows with optimal thicknesses less than 20 nm.

Pyromellitic diimide (PMD) represents the most condensed aromatic diimides characterized by its low price, high electron affinity and transparency, making it an intriguing building block for diverse functional materials.[32] For example, PMD derivatives have

exhibited outstanding performance as n-channel organic semiconductors with electron mobilities approaching 0.1 $cm^2 V^{-1} s^{-1}$ in air.[33,34] More importantly, PMD is a key component of traditional polyimides, which are classified as engineering plastics. These materials are characterized by their outstanding mechanical, chemical, and thermal stability, as well as remarkable resistance to radiation and solvents.[35] Consequently, polyimides hold promise as transparent CIL materials, providing the additional benefit of safeguarding the active layer against external factors like heat, light, and oxygen to enhance the device stability. However, limited focus has been placed on this aspect, potentially due to challenges of conductivity and alcohol processability. Ionenes are a class of polyelectrolytes in which the ionic moieties reside within the polymer backbones rather than as pendant groups.[36] Stemming from their high ionic density, ionenes always exhibit good solubility in polar solvents and they decrease the *WF* of metal electrodes by generating interfacial dipoles. Our recent advances in electroactive ionenes have enhanced their film-forming ability and conductivity, establishing them as compelling CIL materials for OSCs.[37-39] For instance, we have proposed a series of electroactive ionenes containing diazabicyclic (DABC) cation linkage rather than the commonly used ammonium.[37] The optimal electroactive ionene namely NDI-DABC (its chemical structure can be found in **Figure S1**), containing NDI as the π-conjugation, exhibits excellent charge-transport and decent crystallinity, leading to efficient and stable OSCs. However, as its thickness increases to 70 nm, a significant decline in external quantum efficiency (EQE) from 350 to 450 nm can be observed, which is ascribed to the intensive absorption of NDI-based interlayer within this wavelength range, causing a reduction of short-circuit current density (J_{SC}) in solar cell devices. Similar trends are also observed with other PDI and NDI-based CILs.[30,40,41] Besides, the strong absorption of these CILs in 400–600 nm, the most sensitive region to human eyes,[42] will reduce the average transmittance of ST-OSCs. Thus, developing CILs that integrate the synergistic characteristics of polyimides and ionenes offers a compelling and feasible approach to tackle the transparency-electron transport trade-off in current CIL design. However, it is still a grand challenge to achieve the optimal molecular design, since the existing PMD-containing CILs always show inferior thickness tolerance relative to NDI or PDI-based counterparts, due to their undesirable electronic properties.

Herein, we present two innovative polyimide-ionene hybrids (PIIHs), PMD-DI and PMD-PD as CIL materials for OSCs (**Figure 1A**). Through the cost-effective Menshukin polycondensation, PMD motifs are covalently integrated into the ionenes matrix, rending both PIIHs outstanding transparency and alcohol solubility. The design principles of the PIIHs are as follow: (1) Imidazolium cations are incorporated instead of universally employed quaternary

amine cations because imidazole-functionalized CILs are proved to have better film-forming ability and conductivity with respect to amine-functionalized counterparts.[43] (2) By taking advantage of the tailorable structure of electroactive ionenes,[29,37] the PMD content can be easily controlled through judiciously choosing the monomers, providing the opportunity to mediate their film morphology and electronic properties. Our results show that PMD-PD containing higher PMD content shows enhanced conductivity, higher electron mobility, and better organized crystalline structures as thin films than PMD-DI. These advantages support its superiority in modulating the properties of the cathode/active layer interface, mitigating charge recombination, and enhancing charge extraction. Consequently, efficient OSCs have been realized across a broad range of PMD-PD CIL thicknesses (8–65 nm), with a record optimal thickness of 30 nm. The OSCs also exhibit excellent operational stability with a T_{80} (the time required to reach 80% of initial PCE during ageing) lifetime of 1000 h. Notably, PMD-PD is compatible with diverse active layer systems as well as both silver (Ag) and less expensive copper (Cu) electrodes. Remarkable PCEs of 19.91% and 19.29% are achieved in PM6:L8-BO:BTP-eC9 system when pairing with Ag and Cu electrodes, respectively. Furthermore, PMD-PD is well-suited for ST-OSCs by improving PCEs without compromising their transmittances, thus promoting the light utilization efficiency (LUE) of PM6:L8-BO:BTP-eC9-based ST-OSCs up to 4.04% when combined with ultrathin Cu electrodes. These findings position PMD-PD as one of the most promising CIL materials known to date, marking a significant advancement in the organic photovoltaic community.

2. Results and discussion

The PIIHs were prepared by a two-step metal-free synthetic protocol shown in **Scheme S1** with experimental details presented in the Supporting Information. First, the nucleophilic substitution reaction of pyromellitic dianhydride with 1-(3-aminopropyl) imidazole or 3-bromopropylamine afforded intermediates PMD-M or PMD-Br in moderate yields of ~60%. PMD-M was then reacted with 1,3-dibromopropane or PMD-Br using a Menshukin polycondensation to obtain PMD-DI or PMD-PD with yields of 85% and 82%, respectively (**Scheme S1**). The number-average molecular weight (M_n) and polydispersity index ($Đ$) were measured to be 14.9 kDa and 1.01 for PMD-DI, and 16.5 kDa and 1.08 for PMD-PD. The cost (C_g, cost-per-gram) for both PMD-DI and PMD-PD are no more than 1.36 \$ g^{-1} (**Table S1**), one of the most cost-effective aromatic diimides-based interlayer materials reported so far.[31,39,43,44] These PIIHs are soluble in alcohol-based solvents, offering orthogonal solubility to common organic semiconductors to prevent disruption during sequential coating process.

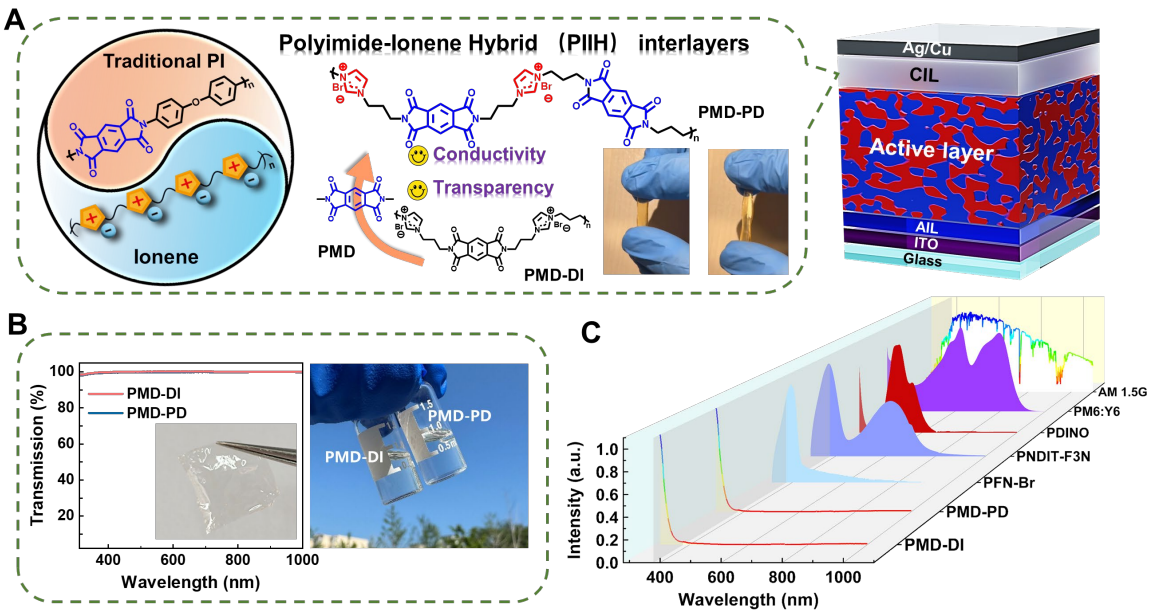

Figure 1. (A) Design motivation and the chemical structures of PIIHs in this work (Insertion: schematic diagrams of the PIIH sample before and after stretching); (B) Left: transmission spectra of PMD-DI and PMD-PD films (50 nm, the photograph of 0.1 mm PMD-PD film is inserted) and Right: the photograph of the PIIHs in solution; (C) UV-*vis*-NIR absorption spectra of the PIIHs. The absorption spectra of some typical CIL materials (PFN-Br, PNDIT-F3N, and PDINO), three typical non-fullerene acceptor-based photoactive layer (PM6:Y6, PM6:BTP-eC9, and PM6:L8-BO:BTP-eC9), and the AM 1.5G spectrum are also included for comparison.

Due to the simplest aromatic structure of a benzene ring in PMD, both PMD-PD and PMD-DI are highly transparent with transmittance surpassing 99.9% from 350 to 1000 nm range (**Figure 1B**). Illustrated in **Figure 1C**, the absorption bands of PMD-DI and PMD-PD are in the ultraviolet region, with onset at 335 nm, corresponding to optical bandgaps (Eg^{opt}s) of 3.70 eV, which is notably higher than those of commonly used PDI and NDI-based interlayers (1.84 and 1.63 eV for PDINO[45] and PNDIT-F3N,[30] respectively), even exceeding that of PFN-Br (2.85 eV), a widely used light-colored CIL material.[46] This feature effectively prevents any potential disruption to the photon absorption of the active layers spanning from the near-ultraviolet to near-infrared regions when used as interlayers.

To verify the effectiveness of these PIIHs as CILs for OSCs, we initially fabricated conventional OSCs with a configuration of ITO/PEDOT:PSS/active layers/PIIHs/Ag (**Figure S1**). Taking the benchmark PM6:Y6 as the active layer, the control devices without CIL (bare Ag) have a quite low PCE of 13.03%, while the efficiencies are boosted substantially to 16.50% and 17.25% when PMD-DI and PMD-PD are inserted, respectively (**Figure 2A** and **Table S2**).

The increase in PCE arises from the concurrent enhancement of the open-circuit voltage (V_{OC}) from 0.793 to 0.849 and further to 0.855 V, the fill factor (*FF*) from 65.94% to 74.41% and then to 76.68%, and J_{SC} from 24.90 to 26.10 and then to 26.31 mA cm^{-2}. The integrated current density values from the EQE spectra are in good agreement with the J_{SC} values obtained from the current density−voltage (*J*−*V*) measurements within 4% error, verifying the accuracy of *J*−*V* measurements (**Figure S2**). The transparent nature of PIIHs is advantageous for thick-film processing. As such, the dependence of PCEs on PIIHs thicknesses were also carefully evaluated. Shown in **Figure 2B** and **Table S3**, the PCE of PMD-DI-based OSCs is highly dependent on the *FF*, evidenced by the fact that the V_{OC} and J_{SC} remain almost consistent throughout entire PMD-DI thicknesses (8−62 nm), while the *FF* decreases from ~ 74% to ~ 64%. In stark contrast, PMD-PD-based OSCs exhibit superior device performance under similar CIL thickness compared to PMD-PD-based devices. Specifically, the PCEs show a progressive enhancement as the PMD-PD thickness increases from 8 to 30 nm, attributed to continuous improvements in J_{SC} and *FF* without effecting the V_{OC}. With the increase of PMD-PD thickness up to 65 nm and a respectable PCE exceeding 15.41% is maintained, representing about 90% of the maximum value (**Figure S3**). As far as we know, the optimal thickness of PMD-PD should be the best among the CIL materials reported to date (**Figure 2C** and **Table S4**), which facilitates its practical application.[47] For comparison, a maximum PCE of 16.24% was recorded with 5 nm of PFN-Br as the CIL, and it quickly dropped to less than 1% as the PFN-Br thickness increased to 17 nm (**Table S3**). The performance of PFN-Br-based devices relies heavily on the thickness of the PFN-Br layer due to its low electron mobility, stemming from the p-type characteristics of the polyfluorene backbone.

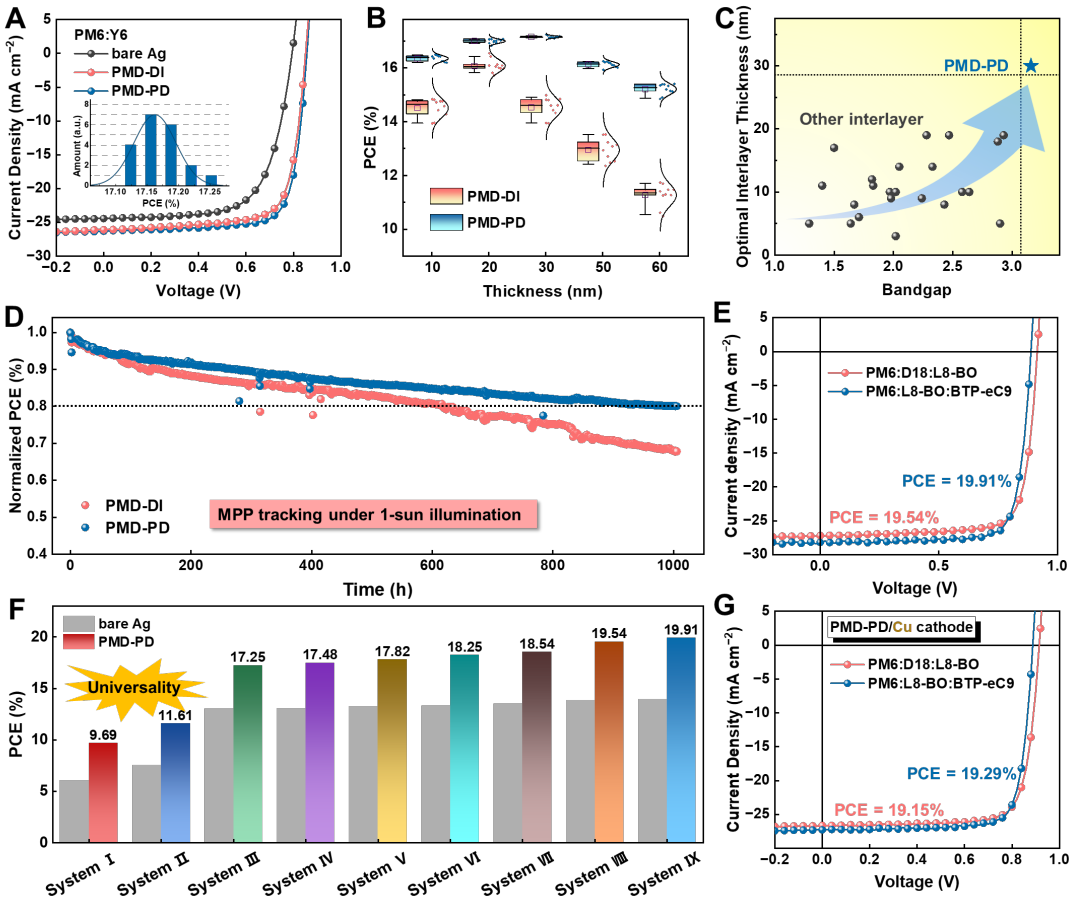

Figure 2. (A) *J*–*V* curves for PM6:Y6-based OSCs without CILs (bare Ag), and with PMD-DI or PMD-PD CILs under optimized thicknesses (Inset: PCE histograms of PMD-PD-based devices); (B) Variation of PCEs as a function of interlayers thicknesses; (C) Optical bandgap against the optimal thicknesses of various CILs diagram; (D) Operational stability of the devices with different CILs; (E) *J*–*V* curves for PM6:D18:L8-BO and PM6:L8-BO:BTP-eC9 -based OSCs with PMD-PD CIL and TBT-L-Br AIL; (F) The summarized efficiency histograms of bare Ag and PMD-PD-based devices with various active layer systems (I: PBDB-T:ITIC; II: PM6:IDIC; III: PM6:Y6; IV: D18:Y6; V: PM6:BTP-eC9; VI: PM6:L8-BO; VII: D18-Cl:N3; VIII: PM6:D18:L8-BO@TBT-L-Br; IX: PM6: L8-BO:BTP-eC9@TBT-L-Br); (G) *J*–*V* curves of PM6:D18:L8-BO and PM6:L8-BO:BTP-eC9 systems with PMD-PD/Cu cathode.

The operational and shelf stability of the OSCs based on PIIH interlayers were further investigated. The operational stability of the devices was assessed by monitoring the performances of encapsulated devices at the maximum power point (MPP) under continuous 1-sun illumination in ambient conditions (**Figure 2D** and **S4**). After ageing for 1000 hours, PMD-DI-based devices experience a 32% decrease in their initial PCE, and a 20% decrease is seen with PMD-PD-based devices. To provide further context, the operational stability of PFN-Br-

based devices was also assessed, showing that the corresponding devices show more significant degradation, with a T_{80} lifetime of merely 250 hours (**Figure S5**). The enhanced stability of the PMD-PD-based OSCs may associate with the suppressed interfacial charge recombination (*vide infra*) and the inherent mechanical properties and photothermal resistance of PIIHs (**Figure S6**).[48] Moreover, in comparision with PMD-DI, the PMD-PD exhibits increased hydrophobicity and enhanced interfacial compatibility with the PM6:Y6 active layer, which is expected to enhance the stability of OSCs (**Figure S7** and **Table S5**).[24,44] Additionally, unencapsulated devices underwent storage in an N_2-filled glovebox for more than 160 days, with the PMD-DI and PMD-PD-based devices maintain 90% and 96% of their initial PCEs, respectively (**Figure S8**).

We next examined the compatibility of PMD-PD with various active layers. In addition to PM6:Y6 discussed above, seven other prominent binary and ternary active layer systems, namely PBDB-T:ITIC, PM6:IDIC, D18:Y6, PM6:BTP-eC9, PM6:L8-BO, D18-Cl:N3, PM6:D18:L8-BO, and PM6:L8-BO:BTP-eC9 were chosen for study (**Figure 2E**, **F** and **Table S6**). The introduction of PMD-PD results in significant enhancements in performances for all systems. Subsequent anode engineering by replacing PEDOT:PSS with TBT-L-Br,[49] the PCE of PM6:L8-BO:BTP-eC9-based devices was improved to 19.91%, with a V_{OC} of 0.886 V, a J_{SC} of 28.19 mA cm^{-2} and a *FF* of 79.64% (**Figure S9** and **S10**). These are the best results for PMD-based CILs and should be one of the most promising outcomes for single-junction OSCs to date. Apart from performance and stability, cost should also be taken into serious consideration for commercialization of organic photovoltaics.[14] Cu, a more cost-effective option compared to the prevalent Ag, can serve as an alternative material for cathode preparation.[24,31] The pairing of PMD-PD with Cu cathode result in high PCEs of 19.15% and 19.29% for the PM6:D18:L8-BO and PM6: L8-BO:BTP-eC9 systems, as shown in **Figure 2G**. Achieving a PCE exceeding 19% is impressive for OSCs utilizing metal electrodes with relatively low price, underscoring the promising application of PMD-PD for cost-effective OSCs (**Figure S11** and **Table S7**).

Given the exceptional transparency of PMD-PD that prevents interference with the human eye response and its applicability to opaque devices, we posit its potential suitability for ST-OSCs (**Figure 3A**).[50-55] Corresponding devices were thus constructed with the configuration of ITO/TBT-L-Br/PM6:BTP-eC9/PMD-PD/Ag (or Cu). It is well known that the formation of smooth ultra-thin top metal electrode is very important to achieve high conductivity and transparency as well as good Ohmic contact. The scanning electron microscopy (SEM) images, as presented in **Figure S12**, convincingly demonstrated the beneficial role of PMD-PD in

ensuring a uniform and continuous morphology of the ultra-thin top metal electrode. ST-OSCs containing PMD-PD interlayers have a significantly enhanced PCE (from 9.32% to 14.57%) with no compromise on the average visible light transmittance (AVT), resulting in a substantial increase in light utilization efficiency (LUE, LUE = PCE×AVT) from 1.60% to 2.49% compared with the bare Ag controls (**Table 1**, **Figure 3B** and **C**). Considering the better transmission to visible light of the Cu cathode and the superior compatibility between PMD-PD and Cu, we advanced to fabricate ST-OSCs by changing Ag electrodes to Cu electrodes with a thickness of 15 nm or 10 nm (**Figure 3D**, **E** and **S13**). This optimization improved LUE values of the devices to 2.80% and 3.64%, respectively, as shown in **Table 1**. For comparison, PFN-Br, one of the most used CILs in ST-OSCs, was also used as the reference.[56] When combined with an ultrathin Cu electrode, inferior PCE (8.65%) and LUE (2.97%) are obtained in the control devices. In contrast, the PMD-PD/Cu (10 nm)-based ST-OSCs containing PM6:L8-BO:BTP-eC9 active layer boost the LUE to 4.04%, affirming the potential of PMD-PD/Cu cathodes for efficient and cost-effective ST-OSCs (**Table 1**).[57] Being distinct from the commonly employed strategies to enhance the LUE of ST-OSCs (such as the active layer optimization, electrode optimization, and optical structure introduction, detailed in **Table S8**), this study seeks to enhance the performance of ST-OSCs through cathode interlayer manipulation by making full use of the merits of the transparent PIIHs, an area that has been relatively overlooked in previous research. Again, the use of cost-effective Cu electrode is anticipated to decrease the overall cost of ST-OSCs with respect to the widely used Ag and Au electrode. **Figure 3F** and **S13** provide the transmittance spectra of all the device components and the transmittance spectra of PMD-PD-based ST-OSCs with various cathode. The reduced J_{SC} and altered shape of the EQE curve in ST-OSCs, in contrast to opaque devices, should originate from the inadequate absorption and diminished light utilization resulting from the thinning of the top metal electrode, which is commonly seen in ST-OSCs. This observation aligns with the transmittance spectra presented in **Figure 3F**. Moreover, its color coordinates (x, y), a critical factor for human visual color perception, is (0.317,0.325), as illustrated on the CIE 1931 chromaticity diagram in **Figure 3G**. This coordinate is very close to the white light region, demonstrating the excellent light transmission of the ST-OSCs.

Table 1. Photovoltaic parameters of ST-OSCs under the illumination of AM 1.5 G, 100 mW cm^{-2}.

Cathode	AVT (%)	V_{OC}[a] (V)	J_{SC}[a] (J_{SC}[b]) (mA/cm^2)	FF[a] (%)	PCE[a] (%)	LUE (%)
Ag[c] 15 nm	17.15	0.695 0.682±0.009	22.21 (21.87) 22.58±0.38	60.34 59.56±0.81	9.32 9.17±0.12	1.60
PMD-PD/ Ag[c] 15 nm	17.11	0.842 0.843± 0.004	22.93 (22.64) 22.89±0.26	75.49 74.41±0.99	14.57 14.36±0.13	2.49
PMD-PD/ Cu[c] 15 nm	19.82	0.841 0.840±0.005	22.31 (21.59) 21.99±0.61	75.31 75.38±0.92	14.12 13.91±0.26	2.80
PMD-PD/Cu[c] 10 nm	35.74	0.844 0.840±0.003	16.65 (16.31) 16.53±0.17	72.42 72.49±0.42	10.19 10.07±0.11	3.64
PFN-Br/Cu[c] 10 nm	34.38	0.819 0.815±0.008	16.25 (16.22) 15.92±0.20	64.97 74.43±0.47	8.65 8.36±0.47	2.97
PMD-PD/Cu[d] 10 nm	32.94	0.869 0.871±0.005	18.90 (18.08) 18.88±0.32	74.64 74.26±0.94	12.26 12.22±0.07	4.04

[a] Average values with standard deviations were obtained from at least ten devices; [b] Calculated J_{SC} from EQE curve; [c] Active layer: PM6:BTP-eC9; [d] Active layer: PM6:L8-BO:BTP-eC9.

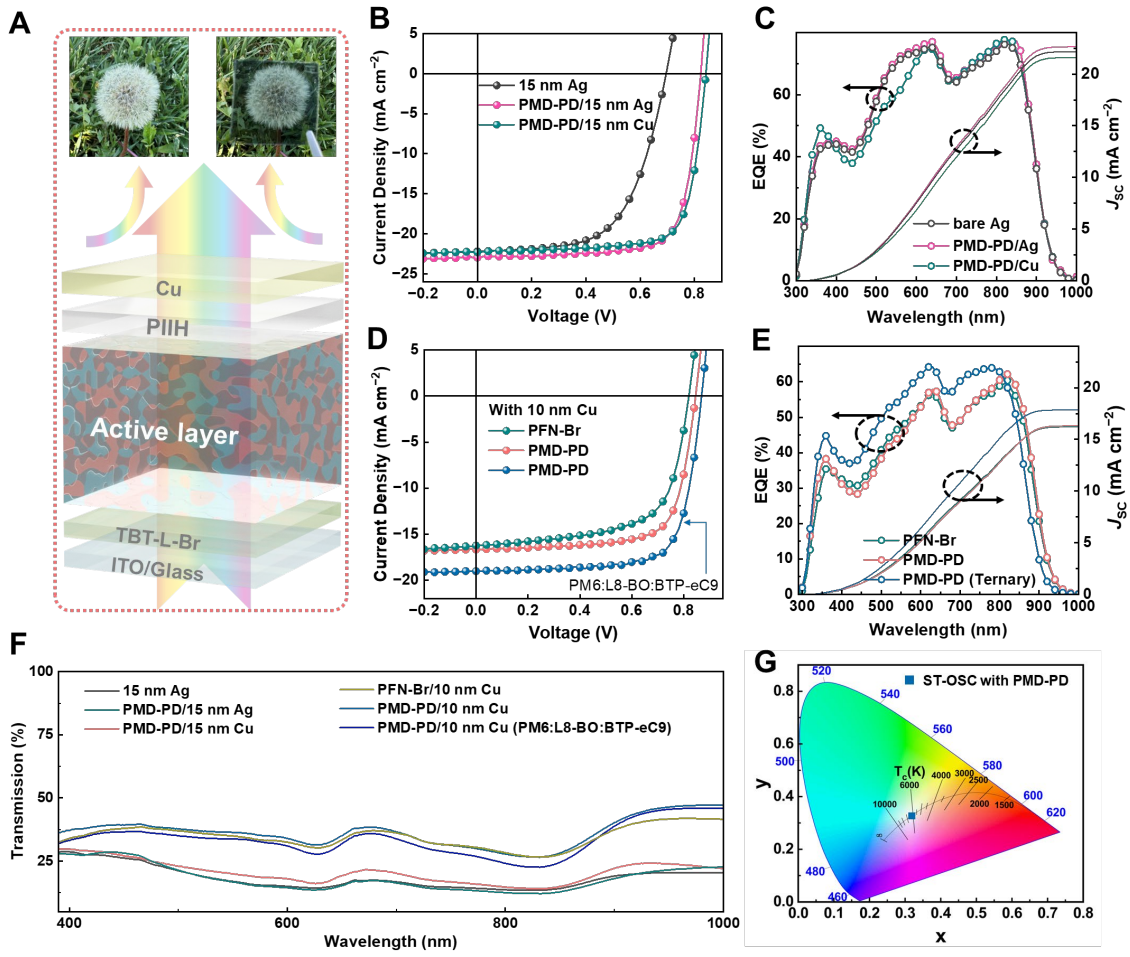

Figure 3. (A) Schematic diagram of the ST-OSCs, photographs were taken without (left) and with (right) a ST-OSC device; (B) $J-V$ and (C) EQE curves of 15 nm Ag, PMD-PD/ 15 nm Ag and PMD-PD/ 15 nm Cu-based ST-OSCs (active layer: PM6:BTP-eC9); (D) $J-V$ and (E) EQE

curves for PFN-Br and PMD-PD-based ST-OSCs with 10 nm Cu cathodes, ternary denotes the PM6:L8-BO:BTP-eC9 active layer; (F) Transmission spectra of PMD-PD-based ST-OSCs with various cathodes; (G) The CIE (x,y) of the device based-PM6:L8-BO:BTP-eC9.

To comprehensively grasp the pivotal role played by the PIIHs in advancing such exciting performances of the OSCs, a series of device characterizations were carried out. It can be seen from the photovoltaic parameters that the J_{SC} of PM6:Y6-based devices only decreased by 0.5 and 0.76 mA cm^{-2} as the thicknesses of PMD-PD and PMD-DI increase to over 60 nm, respectively. Considering the transparent nature of the PIIHs and such minimally reduced J_{SC} of the OSCs with thick PIIHs layers, their potential optical spacer effect was studied. According to the simulated electric field intensity $|E|^2$ of OSCs, introduction of PIIHs interlayers leads to a spatial redistribution of light intensity (**Figure S14** and **S15**).[58] Specifically, as the thickness of PIIHs increases from 0 to 65 nm, the spatial distribution of light intensity aligns more closely with the active layer, which enhances absorption in the active layer to generate more charge carriers. The unique optical spacer effect of PIIHs layers helps offset photocurrent losses when utilized as thick CILs. Moreover, OSCs treated with PMD-PD consistently exhibit higher J_{SC} compared to those with a similar thickness of PMD-DI interlayer. To elucidate the underlying reason, *J*–*V* characteristics of the OSCs in dark conditions were first recorded with the curves shown in **Figure 4A**. The incorporation of PIIHs leads to increased rectification ratios and reduced leakage currents of the OSCs. This outcome indicates a mitigation of charge recombination, particularly evident in PMD-PD-modified devices, aligning with the enhancement of J_{SC}.

Then the function of photocurrent density (J_{ph}) was plotted as effective voltage (V_{eff}) to investigate the impact of PIIHs on exciton dissociation and charge collection.[59] The results, depicted in **Figure 4B**, show that exciton dissociation probability (P_{diss}) values exceeding 97% are observed in all devices. However, the charge collection probability (P_{coll}) value increases from 77.7% in bare Ag-based devices to 86.4% in PMD-DI-based devices and then to 88.9% in PMD-PD-based devices. This suggests that the insertion of PIIHs can enhance charge collection significantly, which is beneficial to boost the *FF*. The charge recombination behavior was investigated through the analysis of *J*–*V* curves at varied illumination intensities (P_{light}s) as depicted in **Figure 4C**.[60] The relationship between J_{SC} and P_{light} can be described by $J_{SC} \propto P_{light}^{\alpha}$, where the power-law component α signifies the extent of bimolecular recombination. The α values of 0.977, 0.985, and 0.992 are obtained for bare Ag, PMD-DI and PMD-PD-based devices, respectively, suggesting a gradually reduced bimolecular recombination. Trap-assisted

recombination (of the Shockley-Read-Hall type) was assessed using the formula of $V_{OC} \propto nkT/q\ln(P_{light})$, where k, T, and q denote the Boltzmann's constant, the Kelvin temperature, and the elementary charge, respectively. The slopes decline drastically from $1.42kT/q$ to $1.15kT/q$ and $1.07kT/q$ for bare Ag, PMD-DI and PMD-PD-based devices, respectively. The results demonstrate effective suppression of trap-assisted recombination with the inclusion of PIIH interlayers, particular in the case of PMD-PD. The charge extraction and recombination processes were also tracked by transient photocurrent (TPC) and transient photovoltage (TPV).[61] At short-circuit conditions, TPC decay traces exhibit decreasing lifetimes in the sequence of bare Ag (0.64 μs), PMD-DI (0.55 μs), and PMD-PD-based devices (0.48 μs), indicating a progressive enhancement in charge extraction efficiency (**Figure 4D**). When operating under open-circuit conditions, the charge carrier lifetime extracted from the TPV decay trace of the PMD-PD-based device (1.97 μs) is notably longer compared to that of the bare Ag and PMD-DI-based devices at 1.00 μs and 1.56 μs, respectively (**Figure 4E**), demonstrating the effectiveness of PMD-PD in mitigating recombination losses. Notably, the PFN-Br-based control presents more severe recombination with respect to PIIH-based devices, thus deteriorating the device performance and stability (**Figure S16** and **S17**). Furthermore, the impedance spectroscopy analysis was conducted to probe the recombination dynamics within the devices with the data listed in **Table S9**. The Nyquist plots and equivalent circuit model in **Figure S18** show a significant decrease in series resistance (R_s) from bare Ag-based devices (96 Ω) to PMD-DI-based devices (85 Ω) and then to PMD-PD-based devices (61 Ω). Additionally, the introduction of PMD-PD results in a more pronounced increase in recombination resistance (R_r) compared to PMD-DI.

Furthermore, capacitance–voltage (C–V) measurements and the corresponding Mott-Schottky analysis were conducted. The built-in voltage (V_{bi}) of devices, as determined by Mott-Schottky analysis, shows a significant rise from 0.48 V (bare Ag-based devices) to 0.71 V and 0.77 V upon the integration of PMD-DI and PMD-PD CILs, respectively (**Figure 4F**). This escalation indicates the establishment of an optimized internal electric field conducive to efficient charge transport and the achievement of higher V_{OC}.[62] Subsequently, thermal admittance spectroscopy (TAS) was performed to examine the trap density at various energy depths.[63] **Figure 4G** illustrates the energetic profile of trap density of states (tDOS) for devices containing PMD-DI and PMD-PD CILs. Within the energy range from 0.28 to 0.48 eV, the tDOS of PMD-PD-based device is approximately one order of magnitude lower and more structured with respect to that with PMD-DI interlayer, indicating a lower defect density by

incorporating PMD-PD interlayer that is advantageous for mitigating charge recombination and improving charge collection efficiency.

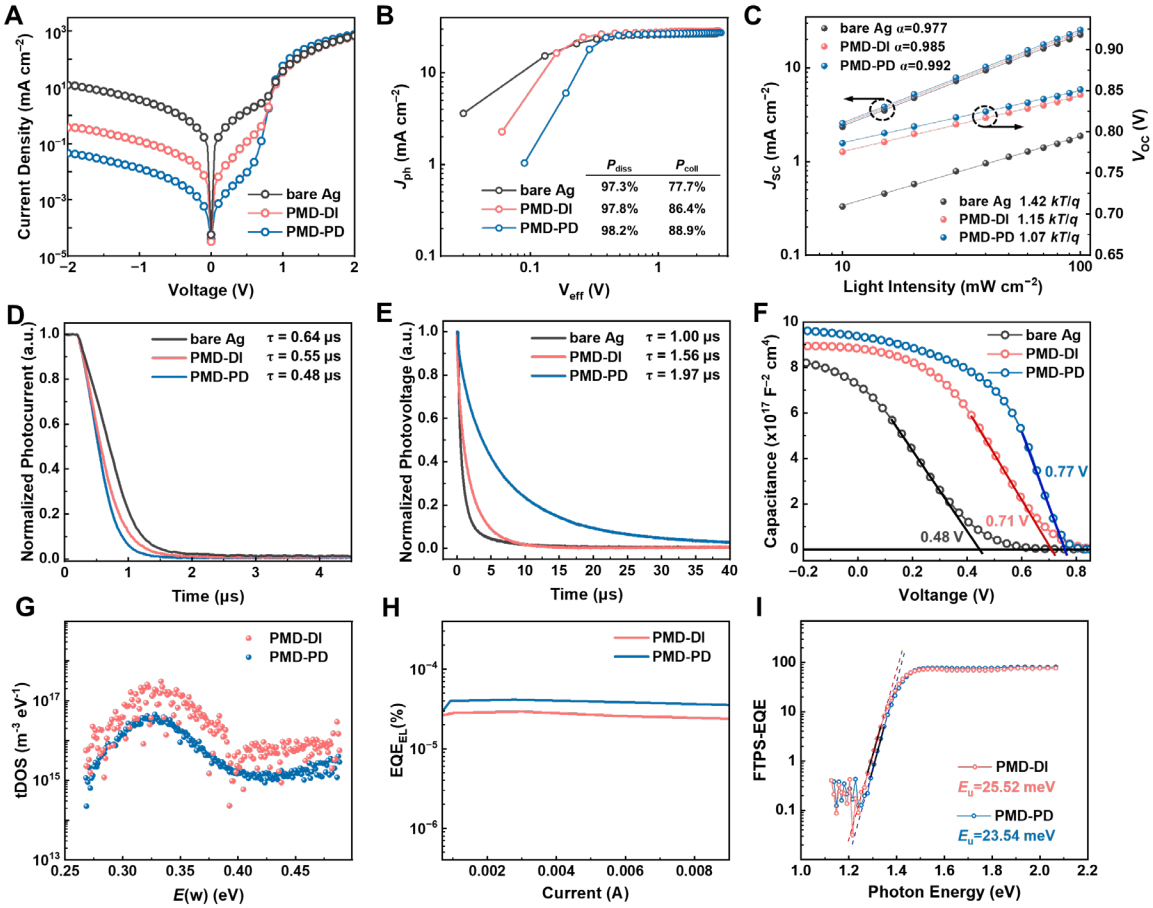

Figure 4. (A) Dark J–V curves; (B) Photocurrent density (J_{ph}) plotted against effective bias (V_{eff}); (C) Light intensity dependence of J_{SC} and V_{OC}; (D) TPC curves; (E) TPV curves; (F) Mott–Schottky characteristics; (G) tDOS spectra; (H) EQE$_{EL}$ spectra; and (I) FTPS-EQE spectra of OSCs based on PM6:Y6 blend containing different CILs.

To elucidate the origin of the higher V_{OC} in PMD-PD-based OSCs than that in PMD-DI-based devices, energy losses (E_{loss}) of the devices containing different PIIH interlayers were analyzed quantitatively based on established methods.[64,65] The PMD-PD-based devices exhibit slightly smaller E_{loss} of 0.562 eV compared to the PMD-DI-based devices with an E_{loss} of 0.573 eV (**Table S10**). Specifically, both types of OSCs deliver the same values of radiative loss above the bandgap (ΔE_1) and radiative loss below bandgap (ΔE_2), while the PMD-PD-based devices exhibit a lower non-radiative loss (ΔE_3) of 0.238 eV in contrast to the PMD-DI-based devices (0.249 eV). This suggests that it is the nonradiative recombination loss that should be responsible for the discrepancy in V_{OC} of the devices. The results were further supported by electroluminescent quantum efficiency (EQE$_{EL}$) measurements. As shown in **Figure 4H**, the

PMD-PD-based devices have a higher EQE_{EL} of 4.0×10^{-5}, resulting in a $q\Delta V_{nr}$ of 0.260 eV (ΔV_{nr} represents non-radiative voltage loss), while the PMD-DI-based devices show a lower EQE_{EL} of 2.8×10^{-5}, corresponding to a higher $q\Delta V_{nr}$ of 0.269 eV. Furthermore, the Urbach energies (E_us) of the devices can be derived by fitting the Fourier transform photocurrent spectroscopy EQE (FTPS-EQE) curves.[66] The E_u values of PMD-DI and PMD-PD-based devices are determined to be 25.52 and 23.54 meV, respectively, indicating that devices integrating PMD-PD have lower energetic disorder (**Figure 4I**). The observations are in line with the decreased nonradiative energy loss of the devices, which should be conductive to affording higher performance.

The superior performances of PMD-PD and PMD-DI-based devices can be associated with the optimized overall properties of these PIIHs, encompassing interfacial modification capability, optoelectronic characteristics, and film morphology, particularly for PMD-PD. Based on the ultraviolet photoelectron spectroscopy (UPS) presented in **Figure 5A**, it is evident that the deposition of PMD-DI and PMD-PD leads to a notable decrease in the *WF* of Ag from 4.51 eV to 3.67 eV and 3.64 eV, respectively, corresponding to the interfacial dipole values of –0.84 eV and –0.87 eV. The scanning Kelvin probe (SKP) measurements confirm the substantial and uniform reduction in the *WF* of the Ag electrode surface on a millimeter scale following the modification with PMD-DI and PMD-PD (**Figure 5B**). Additionally, PMD-PD effectively reduces the *WF* of the Cu electrode from 4.98 eV to 4.34 eV (**Figure S19**). This reduction in the *WF* of metal cathode facilitates the elimination of the Schottky barrier between the active layer and the cathode, a critical factor in enhancing the V_{bi} and establishing Ohmic contact, resulting in enhanced charge transport and collection to enhance the performance and stability of the OSCs (**Figure S20**). The ability of the PIIHs to diminish Schottky barriers was directly assessed by fabricating electron-only devices with a configuration of ITO/Y6/PIIHs/Ag. **Figure 5C** shows that incorporating PMD-DI and PMD-PD substantially boosts electron mobility from 6.13×10^{-6} to 3.94×10^{-4} and 4.63×10^{-4} $cm^2\ V^{-1}\ s^{-1}$, respectively. The two orders of magnitudes of electron mobility improvement hints of the reduced Schottky barrier between Y6 and the PIIHs-modified cathodes.

By analyzing the low binding energy regions of their UPS spectra, the highest occupied molecular orbital (E_{HOMO}) values are determined to be ~ –6.50 eV for both PMD-DI and PMD-PD, significantly lower than those of widely used non-fullerene acceptors (**Figure S21**). Furthermore, the energy levels of the PIIHs were also obtained by electrochemical measurements. The onset of the reduction peaks of the PIIHs were deduced to be –0.71 and –0.67 eV, for PMD-DI and PMD-PD, respectively, leading to the lowest unoccupied molecular

orbital (LUMO) energy levels of −3.64 and −3.68 eV, according to the cyclic voltametric curves (**Figure S22**). Unfortunately, the oxidation peaks related to the PIIHs cannot be observed as the oxidation potential increases to 3.0 V. Therefore, the E_{HOMO} values were calculated according to the formula of $E_{HOMO} = E_{LUMO} - E_g^{opt}$, resulting E_{HOMO} values lower than −7.0 eV. The collaborate results from UPS and CV confirm the low-lying E_{HOMO} of the PIIHs, which is advantageous to block reverse hole transport.

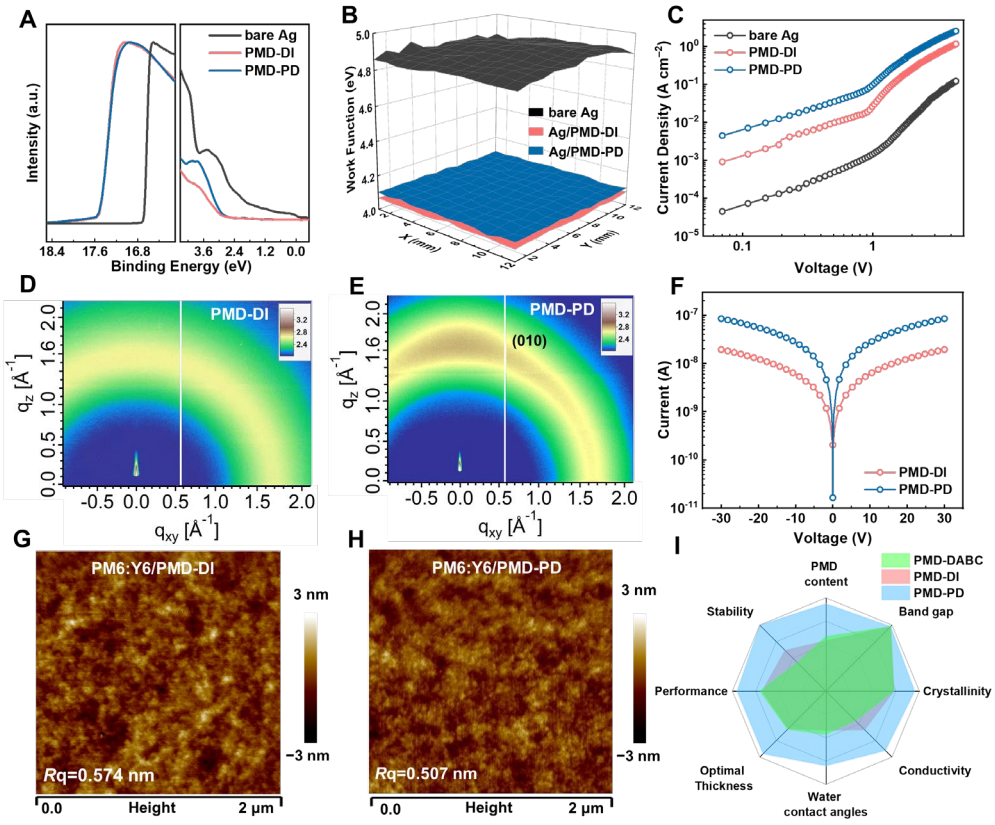

Figure 5. (A) UPS spectra of PMD-DI and PMD-PD-modified Ag and bare Ag substrates; (B) SKP diagrams of Ag substrates with/without modification with PMD-DI and PMD-PD**;** (C) *J*−*V* curves of electron-only devices based on Y6; 2D-GIXD patterns of (D) PMD-DI and (E) PMD-PD; (F) Current–voltage (*I*−*V*) measurements of PMD-DI and PMD-PD films; AFM height images of PM6:Y6 modified by (G) PMD-DI and (H) PMD-PD; (I) Spider chart for deciphering relationship between the properties of the PMD-DABC, PMD-DI, and PMD-PD and the devices performances based on them.

The film morphology of the PIIHs was studied *via* the combination of grazing-incident X-ray diffraction (GIXD) and atomic force microscopy (AFM). Shown in **Figure 5D** and **E**, the PIIHs exhibit distinct crystallinity and stacking as thin films. Specifically, PMD-DI exhibits amorphous nature, evidenced by the diffraction ring at q = 1.61 Å^{-1} (d = 3.90 Å). In contrast,

PMD-PD shows greater crystallinity with a noticeable π–π stacking diffraction peak along the out-of-plane direction at q_z of 1.65 $Å^{-1}$, corresponding to a d spacing of 3.81 Å (**Figure S23**). This characteristic is expected to result not only in an enhanced conductivity and charge mobility of PMD-PD over PMD-DI (**Figure 5F**, **S24** and **Table S11**) but also a reduced E_u and trap density of PMD-PD-based devices with respect to PMD-DI-based devices.[67] Atomic force microscopy (AFM) was then used to study the effect of the PIIH interlayers on the surficial texture of the active layer. As shown in **Figure 5G**, **5H** and **S25**, a notable decrease in roughness (R_q) of the PM6:Y6 photoactive layer, from 1.50 to 0.57 and 0.51 nm can be observed upon coating a thin layer of PMD-DI and PMD-PD, respectively. The results provide compelling evidence for the ability of PIIH interlayers to flatten the surface of active layers, thereby facilitating efficient electron transport at the cathode/active layer interface.

Finally, by leveraging the comprehensive analyses mentioned above, we used a spider chart to visually decipher the interconnection among structural features, optoelectronic properties, morphological characteristics, and device performance of the PIIH interlayer materials (**Figure 5I**). To yield pertinent data to advance rational design methodologies towards more efficient interlayers for practical application, PMD-DABC, a previous reported PMD-based CIL (The chemical structure is shown in **Figure S1**), was also included for comparative analysis. The PMD mass fractions are estimated to be 33.7% and 36.6% for PMD-DI and PMD-DABC, respectively, based on the chemical structures of their repeat units, indicating similar PMD contents. In contrast, PMD-PD has a considerably higher PMD mass fraction of 58.5%, which is beneficial to strengthen the interchain π–π interactions and facilitate the creation of more conductive channels. Therefore, PMD-PD film demonstrates improved crystallinity and superior electrical properties compared to the other two variants, which are vital for improving charge transport efficiency and reducing recombination. This is in line with their distinct performances, especially the substantial performance differences observed in thick interlayers. Furthermore, the higher PMD content in PMD-PD enhances its hydrophobicity and promotes better interfacial compatibility with the active layer, thereby extending the stability of resulting devices. Our findings highlight the significance of augmenting the content of PMD subunits in elevating device performance and stability, and interlayer thickness tolerance without scarifying the transparency.

3. Conclusion

In summary, a range of cost-effective and structurally adjustable PIIHs was developed by covalently integrating PMD subunits into ionene polymers. The resultant PIIHs inherit the advantages of both polyimide and ionenes, showing extremely high transparency and good alcohol processability. PMD-PD, enriched with higher PMD subunit content, exhibits improved crystallinity, greater *WF* tunability, increased electron mobility, thus making it a potential cathode interfacial modifier to enhance electronic communication between the cathode and active layer, contributing to an elevation in V_{bi}, reduction in charge recombination, optimization of light field distribution, and enhancement of charge extraction within the OSCs. Consequently, PMD-PD CIL showcases excellent thickness tolerance with an unprecedent optimal thickness of 30 nm, and ~90% of the optimal device efficiency retained as 65 nm of PMD-PD CILs is incorporated. The PMD-PD-based devices also exhibit excellent stability with operational lifetime extending to 1000 h. Furthermore, PMD-PD matches well with various active layer systems and electrodes, resulting in outstanding PCEs of 19.91% and 19.29% when pairing with Ag and inexpensive Cu cathodes, respectively. Additionally, PMD-PD is well-suited for integration into ST-OSCs without compromising the transparency and color perception, thus yielding an impressive LUE of 4.04% with ultrathin Cu electrodes. This work marks a new phase in developing colorless CIL materials that solves the critical molecular design conundrum of reconciling cost, performance, and stability, a milestone that is necessary for economical, large-scale production of OSCs for various applications.

4. Experimental Section

Please refer to "Supporting Information" for experimental details.

Supporting Information

Supporting Information is available from the Wiley Online Library or from the author.

Acknowledgements

The authors acknowledge the support from National Natural Science Foundation of China (U21A20101, 22305013, and 52473164). W. Liu also thanks the support from Fundamental Research Funds for the Central Universities (buctrc 202144) and the high-performance computing platform of BUCT.

Received: ((will be filled in by the editorial staff))
Revised: ((will be filled in by the editorial staff))
Published online: ((will be filled in by the editorial staff))

References

[1] J. Wang, P. Xue, Y. Jiang, Y. Huo, X. Zhan, *Nat. Rev. Chem.* **2022**, *6*, 614.

[2] Y. Li, F. Qi, B. Fan, K. K. Liu, J. Yu, Y. Fu, X. Liu, Z. Wang, S. Zhang, G. Lu, X. Lu, Q. Fan, P. C. Y. Chow, W. Ma, F. R. Lin, A. K. Y. Jen, *Adv. Mater.* **2024**, *36*, 2313393..

[3] L. Xie, W. Song, J. Ge, B. Tang, X. Zhang, T. Wu, Z. Ge, *Nano Energy* **2021**, *82*, 105770.

[4] J. Song, Y. Li, Y. Cai, R. Zhang, S. Wang, J. Xin, L. Han, D. Wei, W. Ma, F. Gao, Y. Sun, *Matter* **2022**, *5*, 4047.

[5] R. Ma, C. Yan, P. W.-K. Fong, J. Yu, H. Liu, J. Yin, J. Huang, X. Lu, H. Yan, G. Li, *Energy Environ. Sci.* **2022**, *15*, 2479.

[6] X. Zhang, X. Gu, H. Huang, *Acc. Chem. Res.* **2024**, *57*, 981.

[7] Y. Liu, B. Liu, C.-Q. Ma, F. Huang, G. Feng, H. Chen, J. Hou, L. Yan, Q. Wei, Q. Luo, Q. Bao, W. Ma, W. Liu, W. Li, X. Wan, X. Hu, Y. Han, Y. Li, Y. Zhou, Y. Zou, Y. Chen, Y. Li, Y. Chen, Z. Tang, Z. Hu, Z.-G. Zhang, Z. Bo, *Sci. China Chem.* **2022**, *65*, 224.

[8] P. Cheng, G. Li, X. Zhan, Y. Yang, *Nat. Photonics* **2018**, *12*, 131.

[9] G. Zhang, F. R. Lin, F. Qi, T. Heumuller, A. Distler, H. J. Egelhaaf, N. Li, P. C. Y. Chow, C. J. Brabec, A. K. Jen, H. L. Yip, *Chem. Rev.* **2022**, *122*, 14180.

[10] D. Meng, R. Zheng, Y. Zhao, E. Zhang, L. Dou, Y. Yang, *Adv. Mater.* **2022**, *34*, 2107330.

[11] L. Zhu, M. Zhang, J. Xu, C. Li, J. Yan, G. Zhou, W. Zhong, T. Hao, J. Song, X. Xue, Z. Zhou, R. Zeng, H. Zhu, C.-C. Chen, R. C. I. MacKenzie, Y. Zou, J. Nelson, Y. Zhang, Y. Sun, F. Liu, *Nat. Mater.* **2022**, *21*, 656.

[12] C. Guo, Y. Sun, L. Wang, C. Liu, C. Chen, J. Cheng, W. Xia, Z. Gan, J. Zhou, Z. Chen, J. Zhou, D. Liu, J. Guo, W. Li, T. Wang, *Energy Environ. Sci.* **2024**, *17*, 2492.

[13] S. Guan, Y. Li, C. Xu, N. Yin, C. Xu, C. Wang, M. Wang, Y. Xu, Q. Chen, D. Wang, L. Zuo, H. Chen, *Adv. Mater.* **2024**, *36*, 2400342.

[14] X. Yang, Y. Gao, L.-Y. Xu, X. Wu, X. Chen, Y. Shao, B. Xiao, S. Liu, J. Xia, R. Sun, J. Min, *Energy Environ. Sci.* **2024**, *17*, 5962.

[15] Y. Wu, Y. Liu, T. Emrick, T. P. Russell, *Prog. Polym. Sci.* **2020**, *103*, 101222.

[16] H. Tang, Y. Bai, H. Zhao, X. Qin, Z. Hu, C. Zhou, F. Huang, Y. Cao, *Adv. Mater.* **2023**, *36*, 2212236.

[17] Y. Liu, Z. A. Page, T. P. Russell, T. Emrick, *Angew. Chem. Int. Ed.* **2015**, *54*, 11485.

[18] R. Sorrentino, E. Kozma, S. Luzzati, R. Po, *Energy Environ. Sci.* **2021**, *14*, 180.

[19] Z. A. Page, Y. Liu, V. V. Duzhko, T. P. Russell, T. Emrick, *Science* **2014**, *346*, 441.

[20] H. Liu, J. Jiang, S. Dai, L. Yu, X. Zhang, X. Hou, K. Gao, H. Jiang, M. Huang, *Nano Res.* **2024**, *17*, 1564.

[21] Y. Liu, M. Sheri, M. D. Cole, D. M. Yu, T. Emrick, T. P. Russell, *Angew. Chem. Int. Ed.* **2019**, *58*, 5677.

[22] B. Zhang, Y. Zhao, C. Xu, C. Feng, W. Li, X. Qin, M. Lv, X. Luo, X. Qin, A. Li, Z. He, E. Wang, *Adv. Funct. Mater.* **2024**, *34*, 2400903.

[23] Y. Yang, J. Wang, Y. Zu, Q. Liao, S. Zhang, Z. Zheng, B. Xu, J. Hou, *Joule* **2023**, *7*, 545.

[24] C. Zhu, J. Tian, W. Liu, Y. Duan, Y. Song, Z. You, X. Wang, N. Li, X. Zhan, T. P. Russell, Y. Liu, *ACS Energy Lett.* **2023**, *8*, 2689.

[25] Y. Liu, V. V. Duzhko, Z. A. Page, T. Emrick, T. P. Russell, *Acc. Chem. Res.* **2016**, *49*, 2478.

[26] Y. Jiang, Y. Li, F. Liu, W. Wang, W. Su, W. Liu, S. Liu, W. Zhang, J. Hou, S. Xu, Y. Yi, X. Zhu, *Nat. Commun.* **2023**, *14*, 5079.

[27] Z. He, C. Zhong, X. Huang, W. Y. Wong, H. Wu, L. Chen, S. Su, Y. Cao, *Adv. Mater.* **2011**, *23*, 4636.

[28] Y. Zhou, C. Fuentes-Hernandez, J. Shim, J. Meyer, A. J. Giordano, H. Li, P. Winget, T. Papadopoulos, H. Cheun, J. Kim, M. Fenoll, A. Dindar, W. Haske, E. Najafabadi, T. M. Khan, H. Sojoudi, S. Barlow, S. Graham, J.-L. Brédas, S. R. Marder, A. Kahn, B. Kippelen, *Science* **2012**, *336*, 327.

[29] Y. Liu, M. D. Cole, Y. Jiang, P. Y. Kim, D. Nordlund, T. Emrick, T. P. Russell, *Adv. Mater.* **2018**, *30*, e1705976.

[30] Z. Wu, C. Sun, S. Dong, X.-F. Jiang, S. Wu, H. Wu, H.-L. Yip, F. Huang, Y. Cao, *J. Am. Chem. Soc.* **2016**, *138*, 2004.

[31] J. Yao, B. Qiu, Z. G. Zhang, L. Xue, R. Wang, C. Zhang, S. Chen, Q. Zhou, C. Sun, C. Yang, M. Xiao, L. Meng, Y. Li, *Nat. Commun.* **2020**, *11*, 2726.

[32] Q. Zheng, J. Huang, A. Sarjeant, H. E. Katz, *J. Am. Chem. Soc.* **2008**, *130*, 14410.

[33] J. Wang, H. Yu, T. Fu, C. Zhao, H. Yu, Z. Liu, Q. He, D. Zhang, H. Meng, W. Huang, *J. Mater. Chem. C* **2020**, *8*, 7344.

[34] Y. Peng, L. Cao, Z. Li, *Appl. Surf. Sci*. **2017**, *420*, 355.

[35] D.-J. Liaw, K.-L. Wang, Y.-C. Huang, K.-R. Lee, J.-Y. Lai, C.-S. Ha, *Prog. Polym. Sci.* **2012**, *37*, 907.

[36] J. S. Lee, A. Hocken, M. D. Green, *Mol.Syst. Des. Eng.* **2021**, *6*, 334.

[37] Y. Liu, T. P. Russell, *Acc. Chem. Res.* **2022**, *55*, 1097.

[38] M. Liu, P. Fan, Q. Hu, T. P. Russell, Y. Liu, *Angew. Chem. Int. Ed.* **2020**, *59*, 18131.

[39] Z. You, Y. Song, W. Liu, W. Wang, C. Zhu, Y. Duan, Y. Liu, *Angew. Chem. Int. Ed.* **2023**, *62*, 202302538.

[40] J. Yao, S. Ding, R. Zhang, Y. Bai, Q. Zhou, L. Meng, E. Solano, J. A. Steele, M. B. J. Roeffaers, F. Gao, Z.-G. Zhang, Y. Li, *Adv. Mater.* **2022**, *34*, 2203690.

[41] Z. Wang, H. Wang, L. Yang, M. Du, L. Gao, Q. Guo, E. Zhou, *Angew. Chem. Int. Ed.* **2024**, *63*, e202404921.

[42] H. Morkoç, S. N. Mohammad, *Science* **1995**, *267*, 51.

[43] M. Liu, Y. Jiang, D. Liu, J. Wang, Z. Ren, T. P. Russell, Y. Liu, *ACS Energy Lett.* **2021**, *6*, 3228.

[44] X. Li, F. Pan, C. Sun, M. Zhang, Z. Wang, J. Du, J. Wang, M. Xiao, L. Xue, Z. G. Zhang, C. Zhang, F. Liu, Y. Li, *Nat. Commun*. **2019**, *10*, 519.

[45] Z.-G. Zhang, B. Qi, Z. Jin, D. Chi, Z. Qi, Y. Li, J. Wang, *Energy Environ. Sci.* **2014**, *7*, 1966.

[46] F. Huang, H. Wu, D. Wang, W. Yang, Y. Cao, *Chem. Mater.* **2004**, *16*, 708.

[47] W. Liu, J. Wen, H. Yu, X. Zhan, Y. Wang, L. Zhang, Y. Fan, Z. You, Y. Liu, *Angew. Chem. Int. Ed.* **2024**, DOI: 10.1002/anie.202413135.

[48] H. Tang, Y. Bai, H. Zhao, X. Qin, Z. Hu, C. Zhou, F. Huang, Y. Cao, *Adv. Mater.* **2024**, *36*, 2212236.

[49] L. Zhang, Y. Wang, J. Wen, Y. Huang, J. Gao, Y. Duan, S. Park, W. Shin, Z. Ma, M. Liu, S. W. Cho, Y. Park, Y. M. Jung, H. Lee, W. Liu, Y. Liu, *Angew. Chem. Int. Ed*. **2024**, DOI: 10.1002/anie.202408960.

[50] Y. Li, J. Wang, C. Yan, S. Zhang, N. Cui, Y. Liu, G. Li, P. Cheng, *Joule* **2024**, *8*, 527.

[51] W. Liu, S. Sun, L. Zhou, Y. Cui, W. Zhang, J. Hou, F. Liu, S. Xu, X. Zhu, *Angew. Chem. Int. Ed*. **2022**, *61*, e202116111.

[52] D. Wang, H. Liu, Y. Li, G. Zhou, L. Zhan, H. Zhu, X. Lu, H. Chen, C.-Z. Li, *Joule* **2021**, *5*, 945.

[53] V. V. Brus, J. Lee, B. R. Luginbuhl, S. J. Ko, G. C. Bazan, T. Q. Nguyen, *Adv. Mater.* **2019**, *31*, e1900904.

[54] X. Zheng, L. Zuo, K. Yan, S. Shan, T. Chen, G. Ding, B. Xu, X. Yang, J. Hou, M. Shi, H. Chen, *Energy Environ. Sci*. **2023**, *16*, 2284.

[55] H. Yu, J. Wang, Q. Zhou, J. Qin, Y. Wang, X. Lu, P. Cheng, *Chem. Soc. Rev.* **2023**, *52*, 4132.

[56] L. Xiao, Y. Li, H. Zhang, G. Huang, Q. Cheng, S. Li, Y. Zhang, H. Zhou, *Adv. Mater.* **2023**, *36*, 2303844.

[57] X. Huang, X. Ren, Y. Cheng, Y. Zhang, Z. Sun, S. Yang, S. Kim, C. Yang, F. Wu, L. Chen, *Energy Environ. Sci.* **2024**, *17*, 2825.

[58] J. Y. Kim, S. H. Kim, H. H. Lee, K. Lee, W. Ma, X. Gong, A. J. Heeger, *Adv. Mater.* **2006**, *18*, 572.

[59] J. L. Wu, F. C. Chen, Y. S. Hsiao, F. C. Chien, P. Chen, C. H. Kuo, M. H. Huang, C. S. Hsu, *ACS Nano* **2011**, *5*, 959.

[60] A. K. K. Kyaw, D. H. Wang, V. Gupta, W. L. Leong, L. Ke, G. C. Bazan, A. J. Heeger, *ACS Nano* **2013**, *7*, 4569.

[61] S. Wood, J. C. Blakesley, F. A. Castro, *Phys. Rev. Appl.* **2018**, *10*, 024038.

[62] Q. Liao, Q. Kang, Y. Yang, C. An, B. Xu, J. Hou, *Adv. Mater.* **2020**, *32*, e1906557.

[63] Y. Shao, Z. Xiao, C. Bi, Y. Yuan, J. Huang, *Nat. Commun.* **2014**, *5*, 5784.

[64] D. Qian, Z. Zheng, H. Yao, W. Tress, T. R. Hopper, S. Chen, S. Li, J. Liu, S. Chen, J. Zhang, X. K. Liu, B. Gao, L. Ouyang, Y. Jin, G. Pozina, I. A. Buyanova, W. M. Chen, O. Inganas, V. Coropceanu, J. L. Bredas, H. Yan, J. Hou, F. Zhang, A. A. Bakulin, F. Gao, *Nat. Mater.* **2018**, *17*, 703.

[65] K. Vandewal, J. Benduhn, V. C. J. S. E. Nikolis, *Sustainable Energy Fuels* **2018**, *2*, 538.

[66] Z. Zhang, Y. Li, G. Cai, Y. Zhang, X. Lu, Y. Lin, *J. Am. Chem. Soc.* **2020**, *142*, 18741.

[67] Z. Fu, J. W. Qiao, F. Z. Cui, W. Q. Zhang, L. H. Wang, P. Lu, H. Yin, X. Y. Du, W. Qin, X. T. Hao, *Adv. Mater.* **2024**, *36*, 2313532.

Novel polyimide-ionene hybrids that exhibit desirable alcohol processability, conductivity, transparency, and metal/semiconductor interface modification ability are furnished by melding pyromellitic diimides into ionene backbones. These merits render them universal cathode interlayer materials with outstanding thickness tolerance, leading to not only highly efficient and stable opaque devices but also high-performance semi-transparent devices even when pairing with low-cost Cu electrodes.

Transparent and Conductive Polyimide-Ionene Hybrid Interlayers for High Performance and Cost-Effective Semi-transparent Organic Solar Cells

Z. You, J. Wen, W. Liu*, Z. Fink, X. Wu, H. Seong, Y. Wang, L. Zhang, X. Wang, T. P. Russell and Y. Liu*